Room temperature ammonia gas sensing characteristics of copper oxide-tin oxide composite thin films prepared by radio frequency magnetron sputtering technique

S. R. Cynthia[1], R. Sivakumar[2,*] , C. Sanjeeviraja[3], C. Gopalakrishnan[4], and K. Jeyadheepan[5]

[1] Department of Physics, Alagappa Chettiar Government College of Engineering and Technology, Karaikudi 630003, India
[2] Department of Physics, Directorate of Distance Education, Alagappa University, Karaikudi 630003, India
[3] Department of Electronics and Communication Engineering, Alagappa Chettiar Government College of Engineering and Technology, Karaikudi 630003, India
[4] Department of Physics and Nanotechnology, SRM Institute of Science and Technology, Kattankulathur 603203, India
[5] School of Electrical and Electronics Engineering, SASTRA Deemed to be University, Thanjavur 613401, India

ABSTRACT

In this work, thin films of composite copper oxide-tin oxide [$CuO:SnO_2$ (1:1)] were prepared by radio frequency magnetron sputtering technique at room temperature on quartz glass substrates. X-ray diffraction study revealed that the as-deposited films were amorphous in nature and the crystallinity of the films was obtained by annealing the films at 1000 °C. The hexagon rod-like structure, dews-like particles and cylindrical-shaped particles were observed in surface morphological study. The X-ray photoelectron spectroscopic study confirmed the formation of Cu^{2+} and Sn^{4+} states in the deposited films. The decrease in optical energy band gap with increase in RF power and annealing temperature may be due to the creation of localized states near the band edges of $CuO:SnO_2$. The gas sensing characteristics of the films were analysed by recording the electrical resistance variation of the films in the presence/absence of various concentrations of NH_3 gas at room temperature. The $CuO:SnO_2$ film exhibited a highest sensing response of 3838 for 125 ppm of NH_3 gas at room temperature. The film sustained its initial sensor response even after 6 months period for 5 repeated cycles, which ascertained the stability and repeatability of $CuO:SnO_2$ thin film based gas sensor.

Address correspondence to E-mail: krsivakumar1979@yahoo.com

1 Introduction

The atmospheric pollution from automobiles and industrial exhausts has become a global issue. For the survival of the living beings and for the better control of the environment, the detection of toxic, hazardous, combustible gases have become an indispensable for human beings. Among the various toxic gases, NH_3 gas is a pungent odour irritant gas and exposure to NH_3 may lead to skin, eye injuries and lung damage. The highly water soluble nature of NH_3 gas makes to absorb quickly onto the mucosal membrane and skin, which in turn reacts with water to form highly irritant and caustic ammonium hydroxide. However, the extent of the damage depends on the duration of exposure to the gas and the concentration of the gas [1]. The threshold limit for NH_3 specified by the Occupational Safety and Health Administration (OSHA) in the work place is 50 ppm [2]. Since the exposure of NH_3 is a risk to human health and environment, an accurate measurement of NH_3 leak is mandate to protect the human beings and also our environment from the fatal accidents caused by over the exposure to NH_3 in areas such as farming, automotive industries and chemical industries which are the major sources of NH_3 [3].

To detect gases, metal oxide based chemical sensors have been extensively used in view of the fact that the electrical conductivities of semiconducting metal oxide changes with the composition of the gas atmosphere surrounding them [4]. In addition, the metal oxide chemical sensors especially for the detection of NH_3 gas have gained more attention of the researchers because of their main advantages such as low cost, low power consumption, high sensitivity and miniature in size [5]. However, most of the metal oxide NH_3 sensors operate at high temperature. For instance, Pt-loaded WO_3 films showed a response of 8.6 towards 50 ppm of NH_3 at 300 °C [6]. The WO_3 nanoflakes prepared by hydrothermal method showed a high selectivity towards NH_3 at 200 °C [7]. In addition, Li et al. [8] reported that the ZnO thin film prepared by sol–gel method showed a sensor response of 57.5% towards 600 ppm of NH_3 at an operating temperature of 150 °C. Further, direct current reactive magnetron sputtered TiO_2 thin film showed the high sensitivity to NH_3 at an operating temperature of 250 °C [9]. These high temperature operation gas sensors require external heater and excess electric power and also high temperature may affect the performance of resultant sensors.

The sensor operating at room temperature can be achieved by preparing a suitable material with superior electrical, optical, structural and surface morphological properties [10]. In this regard, combination of two different metal oxides in completely mixed form will help to achieve a system with good physical, chemical and electrical properties. Further, mixing of p-type and n-type metal oxide semiconductors leads to the formation of p-n heterojunction between these surfaces, which in turn enhance the sensing property even at room temperature [11]. In this aspect, CuO is a p-type semiconductor with a narrow energy band gap of 1.2 eV and it has been widely used in the field of gas sensor. For examples, Samarasekara et al. [12] reported that the sputtered copper oxide thin film acted as a prime candidate for CO_2 sensor. Nano-bitter gourd-like structured CuO exhibited a high response and good selectivity towards H_2 gas at 200 °C [13]. Moreover, Ponmudi et al. [14] suggested that the CuO mixed metal oxide has a very less effect of humidity on the NH_3 sensing behaviour at room temperature. On the other hand, n-type semiconducting SnO_2 with a wide energy band gap of 3.6 eV [15] is also a well-known material for its application in the field of gas sensing. The mixed phase SnO_2 exhibited a high response to ethanol [16]. Also, Phouc et al. [17] have developed SnO_2 porous nanofibers by electro spinning method and reported that the product has a highest response to H_2S at an operating temperature of 200 °C. Further, the porous SnO_2 films with rich oxygen vacancies showed a high response to triethylamine [18].

It was reported that the equally mixed CuO with Cr_2O_3 [19] and with Al_2O_3 [20] showed a good response towards ammonia gas at room temperature. Hence, the authors would like to modify the combination of CuO with other metal oxide (SnO_2, a good gas sensing candidate) in order to enhance the sensing characteristics further. The notable sensitivity of SnO_2 and the outstanding promotion action of CuO have greatly attracted the research community towards the composites of CuO and SnO_2. Habubi et al. [21] studied the properties of SnO_2-CuO mixed films and found that the increase in thickness of the films have an influence on the microstructure, optical and electrical properties. Xue et al. [22] formed core/shell PN junctions by coating p-type CuO nanoparticles over n-type SnO_2 nanorods and reported that

hetrostructured nanomaterials are promising candidate for high performance gas sensor. Verma et al. [23] said that the incorporation of CuO into SnO_2 enhanced the sensing response of the film towards H_2S gas molecules. In addition, Park et al. [24] showed that porous SnO_2-CuO nanotube enhanced the sensing response towards H_2S gas. Further, Liu et al. [25] reported that the addition of Cu improved the gas sensing performance of SnO_2 thin films in the H_2S gas detection. Even though lot of works have been reported on CuO:SnO_2 composite film, the gas sensing behaviour was not well established for various gas analytes especially for NH_3 gas. To the best of our knowledge, this is the first report on the combination of mixed CuO:SnO_2 (1:1) composite thin film prepared by radio frequency (RF) magnetron sputtering technique for NH_3 gas sensing application at room temperature operating condition.

In the present work, thin films of CuO:SnO_2 (1:1) were prepared by RF magnetron sputtering technique. RF magnetron sputtering is preferred due to its high deposition rate, film growth at relatively low substrate temperature, high stability and suitable adhesion of the films on the substrate. The prepared films were annealed at 500 °C and 1000 °C. The structural, morphological, optical, vibrational and electrical properties of CuO:SnO_2 films were studied. The gas sensing property of optimized film was studied for NH_3 gas analyte at room temperature.

2 Experimental work

2.1 Target preparation

In this work, a sputtering target of CuO:SnO_2 was prepared in 1:1 atomic ratio. The target of CuO:SnO_2 was prepared by thoroughly mixing the powders of CuO and SnO_2 (both with 99.99% purity, Sigma Aldrich) with the atomic ratio of 1:1 and mixed well using the ball miller by adding polyvinyl alcohol (PVA) as a binder for 20 h. The mixture of CuO:SnO_2 was pelletized (dimension of 50 mm diameter and 5 mm thickness) with a pressure of 400 KN using hydraulic pelletizer. The pelletized target was sintered at 1000 °C for 4 h.

2.2 Thin film preparation

Thin films of CuO:SnO_2 (1:1) were prepared on well cleaned quartz glass plates by radio frequency (RF) magnetron sputtering technique (HINDHIVAC; Planar magnetron RF/DC sputtering unit; Model-12″MSPT). The substrates were placed 6 cm apart from the target. The chamber base pressure was maintained as 1×10^{-6} mbar and the working pressure was 1×10^{-3} mbar upon the introduction of high purity argon gas (99.999%) as sputtering gas inside the chamber with a flow rate of 25 sccm using mass flow controller. Thin films of CuO:SnO_2 (1:1) were deposited with the sputtering powers of 50 W, 100 W and 150 W at room temperature (RT) for 10 min. The deposited films were further annealed at 500 °C and 1000 °C for one hour. The thickness (measured by surface profilometer (Mitutoyo, SJ-301)) of as-deposited films with 50 W, 100 W and 150 W RF power is varied as 380 nm, 550 nm, and 830 nm, respectively. In general, the high RF power favours the ionization rate of argon gas and thereby more number of atoms can be ejected from the target material. This leads to the increase in film thickness with RF power. Table 1 shows the thickness values of as-deposited and annealed films. A very small reduction in thickness of CuO:SnO_2 film was observed after the annealing treatment, which may be due to the effect of compact nature of the film.

Table 1 Variation of thickness of the CuO:SnO_2 (1:1) films by the effects of RF power and annealing temperature

Sample preparation condition	Thickness (nm)
As-deposited	
50 W	380
100 W	550
150 W	830
Annealed at 500 °C	
50 W	372
100 W	537
150 W	819
Annealed at 1000 °C	
50 W	366
100 W	532
150 W	810

2.3 Gas sensing measurement

For gas sensing measurement, the sensor element ($CuO:SnO_2$ thin film with 2 cm × 1 cm size) was placed in a chamber of 6 L capacity with gas inlet and outlet arrangements. Ohmic contact between the sensing film and the probe was made using silver paste on the edges of the sensing film. The temperature of the chamber was controlled with a PID temperature controller and the working temperature was maintained at room temperature (RT, 25 °C). The gas sensing setup was equipped with digital source meter (KEITHLEY 2400) and the entire experimental activity was controlled by a computer running with GUI developed in LabVIEW.

The base resistance of the sensing element was measured in an ambient air; after the steady state was reached the gas was injected into the chamber to measure the change in resistance in the sensing element. During measurement, the chamber was kept air tight by closing all the valves to avoid the leakage of gas. After the completion of the measurement a rotary pump was used to wipe out all the gases inside the chamber.

The concentration of testing gas was calculated using the following relation [26],

$$C_{ppm} = \frac{\delta \times V \times R \times T}{M \times P_b \times V_b} \times 10^6 \quad (1)$$

where δ is the density of testing gas (in g ml^{-1}), V is the volume of the injected test gas (in μL), R is the universal gas constant (8.415 J mol^{-1} K^{-1}), T is the sensor temperature (in K), M is the molecular weight of the testing gas (in g mol^{-1}), P_b is the chamber pressure, and V_b is the volume of the chamber (in litres).

2.4 Characterization

The structural property of the prepared $CuO:SnO_2$ (1:1) films was analyzed by X-ray diffraction (XRD) (X'Pert Pro PANalytical, The Netherlands) using Cu-Kα radiation source with λ = 1.5418 Å operating at 40 kV and 30 mA. The surface morphology of the films was examined by scanning electron microscope (SEM) (JEOL—JSM—6390LV) and atomic force microscope (AFM) (Agilent Technologies, USA, 5500 series). The elements present in the films were examined with the help of energy dispersive X-ray analysis (EDX) (OXFORD XMX N) and X-ray

photoelectron spectroscopy (XPS) (PHI—VERSAPROBE III). The optical properties of films were studied using UV–visible NIR spectrophotometer (LAB INDIA, UV3000$^+$) and photoluminescence spectroscopy (PL) (Varian Cary Eclipse). The vibrational property of the film was done using Fourier transform infrared spectroscopy (FTIR) (Thermo Nicolet 380) and the electrical properties of the films were studied with the help of four probe attached with digital source meter (KEITHLEY 2400). Finally, the sensing behaviour of as-deposited and annealed (at 1000 °C) films prepared with 150 W RF power was analysed for various gas analytes including NH_3 by adopting the experimental procedure discussed in Sect. 2.3.

3 Results and discussion

3.1 XRD analysis

The XRD patterns of the CuO powder, SnO_2 powder and the synthesized $CuO:SnO_2$ mixed oxide are shown in the Fig. 1. The XRD pattern of CuO powder shows high intense peaks at 2θ = 35.61°, 38.77°, 48.72°, 58.07° and 68.06° which correspond to the reflection planes (11–1), (111), (20–2), (202) and (022) of monoclinic structure (JCPDS card number 48–1548). On the other hand, the XRD pattern of SnO_2 powder shows well-defined peaks at 2θ = 26.64°, 33.93°, 37.99°, 51.77°, 54.79°, 61.88°, 64.79°, 65.94°, 71.33° and 78.72° are corresponding to (110), (101),
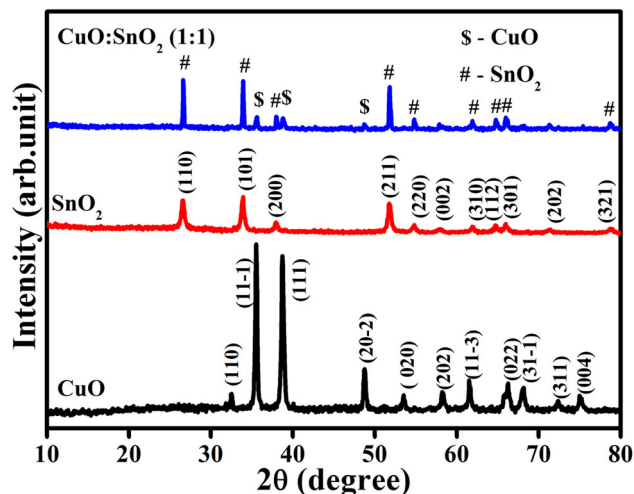

Fig. 1 X-ray diffraction patterns of CuO powder, SnO_2 powder and $CuO:SnO_2$ (1:1) composite oxide

(200), (211), (220), (310), (112), (301), (202) and (321) orientations of tetragonal structure SnO$_2$ (JCPDS card number 88-0287). The XRD pattern of sputtering target has the SnO$_2$ peaks along with only three major peaks of CuO with less intensity. This result revealed the proper mixing of CuO into SnO$_2$ matrix and confirms the formation CuO:SnO$_2$ composite. Also the presence of CuO peak along with the SnO$_2$ peak shows the coexistence of both CuO and SnO$_2$ phases which may provide the possibility of p-n hetero-junction formation between CuO and SnO$_2$ [27]. Table 2 shows the comparison of observed 2θ values of CuO, SnO$_2$ and target material along with JCPDS data. Figure 2 shows the XRD patterns of CuO:SnO$_2$ thin films deposited on quartz glass substrate with the sputtering power of 50, 100 and 150 W and subsequently annealed at 500 °C and 1000 °C. The absence of sharp diffraction peaks in the as-deposited films confirmed the amorphous nature. This is because when the films deposited at RT, the collision relaxation period may not be long enough for the atoms to arrive to the ordered phase as the atom do not gain enough kinetic energy from atomic collision [28]. In addition, the amorphous behaviour was noticed for the films annealed at 500 °C. When the annealing temperature was raised to 1000 °C, the films deposited at 100 W and 150 W showed sharp intense peaks pertaining to CuO and SnO$_2$, which confirmed the polycrystalline nature of CuO:SnO$_2$

composite film. The film deposited at 150 W showed high intense peaks than the film deposited at 100 W. This increase in intensity of the peaks may be due to the improvement in crystallinity and grain size of the film with increase in film thickness at higher RF sputtering power [29]. It is also observed that the preferential growth of the annealed films were along (100) plane. This c-axis growth can provide out-growth formation which would be the reason for surface roughness [30].The average crystallite size of the film prepared at 150 W RF power was calculated by Scherrer's formula [31],

$$d = \frac{K\lambda}{\beta \cos\theta} \tag{2}$$

where d is the crystallite size, K is the Debye–Scherrer's constant, λ is the wavelength of the X-ray radiation (CuKα = 1.5418 Å), β is the full width at half maximum, and θ is the Bragg's angle. The average crystallite size of the film annealed at 1000 °C is 38 nm.

3.2 Surface morphology and compositional analysis

The surface morphology of the prepared sputtering target and the films was analysed using the scanning electron microscopy (SEM) and the images are shown in Fig. 3. The micrograph of the CuO:SnO$_2$ (1:1) target material possesses hexagon rod-like structure as

Table 2 Comparison of observed 2θ values of CuO and SnO$_2$ powders with CuO:SnO$_2$ (1:1) composite oxide along with the JCPDS data

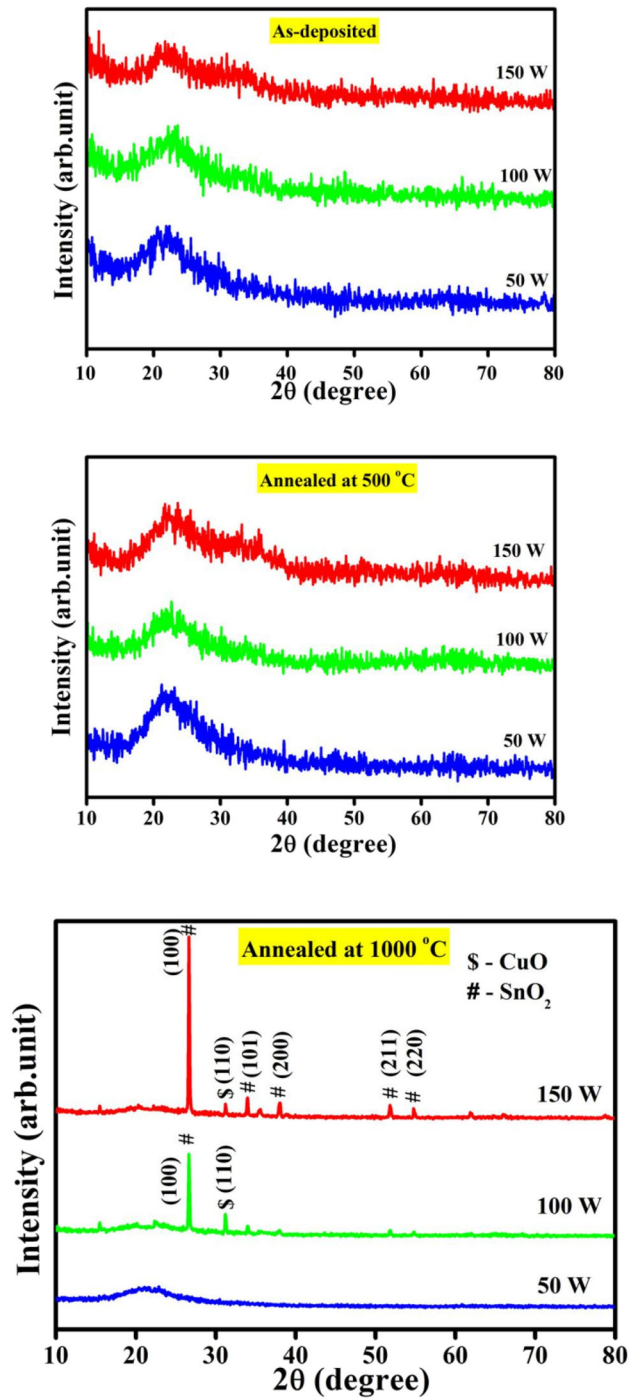| JCPDS 2θ of CuO (deg.)	Observed 2θ of CuO powder (deg.)	JCPDS 2θ of SnO$_2$ (deg.)	Observed 2θ of SnO$_2$ powder (deg.)	Observed 2θ of CuO:SnO$_2$ (1:1) target (deg.)
32.536	32.559	26.589	26.577	26.641
35.574	35.539	33.877	33.898	33.932
38.742	38.722	37.956	37.878	35.612
48.759	48.732	51.777	51.778	37.997
53.533	53.491	54.762	54.783	38.774
58.317	58.263	57.872	57.874	48.721
61.581	61.566	62.607	62.037	51.817
65.873	65.737	64.741	64.748	54.792
66.282	66.225	65.970	66.013	58.077
68.187	68.092	71.279	71.408	61.887
72.441	72.404	78.714	78.835	64.741
75.049	75.084	–	–	65.948
–	–	–	–	68.067
–	–	–	–	71.336
–	–	–	–	78.724

Fig. 2 X-ray diffraction patterns of as-deposited and annealed (at 500 °C and 1000 °C) CuO:SnO$_2$ films prepared with 50 W, 100 W and 150 W RF power
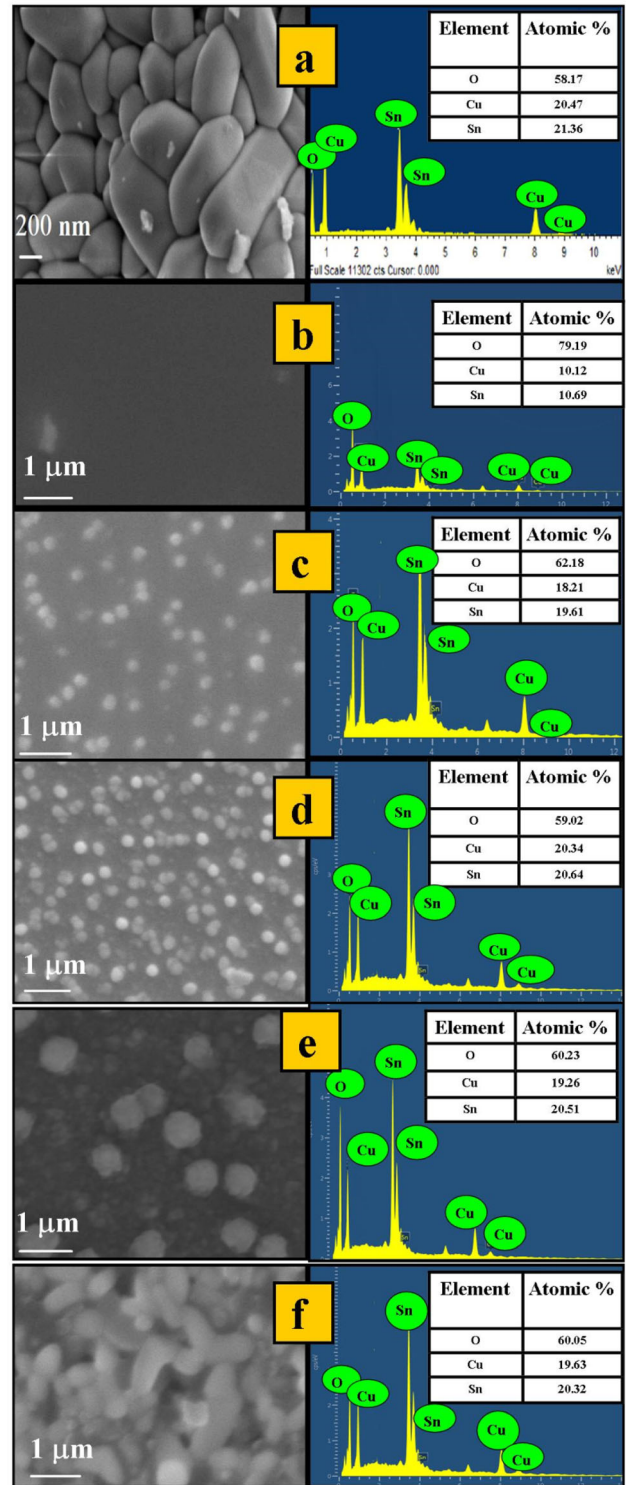

Fig. 3 SEM micrographs and EDX spectra of **a** sputtering target and films deposited with **b** 50 W: as-deposited, **c** 100 W: as-deposited, **d** 150 W: as-deposited, **e** 150 W: annealed at 500 °C and **f** 150 W: annealed at 1000 °C

shown in Fig. 3a. The surface morphology of as-deposited CuO:SnO$_2$ (1:1) films are shown in Fig. 3b–d. The film deposited at 50 W RF power shows no visible particles. Dews-like particles are sparingly present in the films deposited at 100 W and more

numbers of visible particles are seen for 150 W prepared sample. This may be due to the fact that more number of particles would be ejected from the CuO:SnO$_2$ (1:1) target at higher RF power, which in turn leads to the enhancement in film thickness (Table 1). All the films exhibited a uniform surface without any cracks. The SEM images of the film deposited with 150 W RF power and annealed at 500 °C and 1000 °C are shown in Figs. 3e, f, respectively. The 500 °C annealed sample shows the complete formation of larger sized spherical particles all over the surface of the substrate (Fig. 3e), whereas the elongated cylindrical-like structure was seen for the film annealed at 1000 °C as shown in Fig. 3f. The identical morphological variation was seen in the atomic force microscopic (AFM) images of the as-deposited and annealed (at 500 °C and 1000 °C) CuO:SnO$_2$ films prepared with 150 W RF power as shown in Fig. 4. One can observe that the root-mean-square surface roughness (R$_{rms}$) of the films increase with an increase in annealing temperature. For instance, the as-deposited film has the R$_{rms}$ of

23.9 nm and it increases to 48.3 nm and 54 nm when the film was annealed at 500 °C and 1000 °C, respectively. The increase in grain size and the surface roughness of the films with annealing temperature are expected to provide more number of adsorption sites for the atmospheric oxygen [32]. Therefore, the film annealed at 1000 °C possesses a favoured structure for gas sensing.

The EDX spectra of sputtering target and the deposited films are presented along side in Fig. 3, which confirmed the purity of the samples. The stoichiometric nature of the target is confirmed from the atomic % of elements present in target (inset of EDX spectrum in Fig. 3a). The CuO:SnO$_2$ (1:1) film deposited at 50 W RF power has the low atomic percentage ratio of Sn and Cu and as the RF power increases the ratio between Sn and Cu is also increased. This is because of the ejection of more number of particles from the sputtering target at higher RF power [33]. The film deposited with 150 W RF power has close stoichiometry as that of the sputtering target.
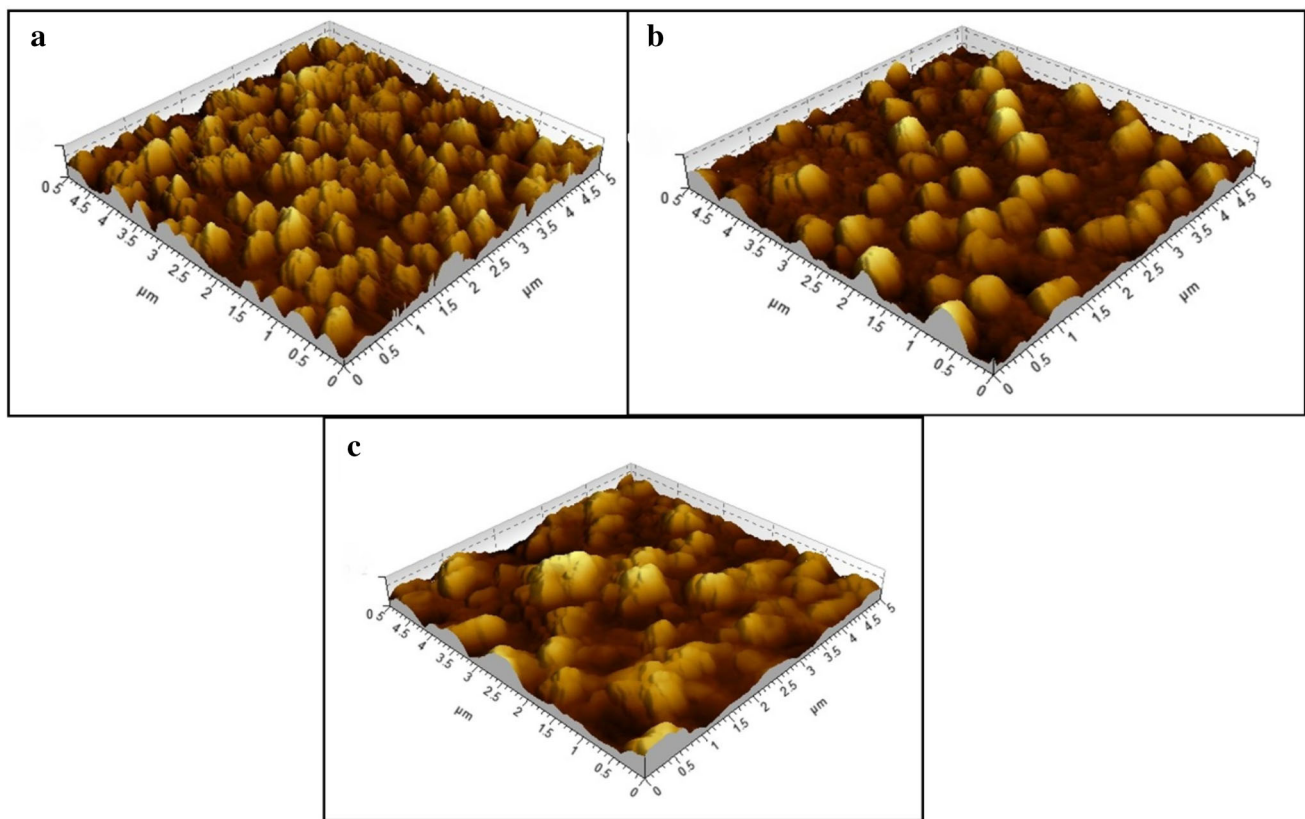

Fig. 4 Three-dimensional (5 μm × 5 μm) AFM scan images of CuO:SnO$_2$ films deposited with 150 W RF power **a** as-deposited, **b** annealed at 500 °C and **c** annealed at 1000 °C

The XPS survey scan and core level (Cu, Sn, O) spectra of CuO:SnO$_2$ thin film deposited with 150 W RF power and annealed at 1000 °C are shown in Fig. 5. Only Cu, Sn, and O elements are present in the spectrum, which further substantiate the films was free from contamination. The presence of C1s peak was used to correct the charge induced shift [20]. In the core level spectrum of Cu, the peaks with binding energies of 932.9 eV and 952.9 eV are assigned to Cu 2p$_{3/2}$ and Cu 2p$_{1/2}$, respectively. The satellite peaks observed at 935 eV, 940.38 eV, 944.9 eV, and 949.7 eV are the characteristic ones of CuO, which indicates the Cu^{2+} state of CuO phase [34]. On the other hand, two broad peaks at 486.6 eV and 495 eV are observed in the deconvoluted core level spectrum of Sn. The separation energy of 8.4 eV specifies the existence of Sn^{4+}. The spin orbit splitting energy of 8.4 eV is in agreement with literature value [35]. The asymmetric O1s peak is analysed after deconvolution into two peaks having binding energies of 530.5 eV and 532.8 eV as shown in Fig. 5. The peak at lowest binding energy (530.5 eV) is due to the lattice oxygen in the metal oxide and the peak at the binding energy of 532.8 eV is assigned to the surface-adsorbed oxygen [36].

3.3 UV–visible NIR spectrophotometer study

The effect of RF power on optical transmission spectra of as-deposited and annealed (500 °C and 1000 °C) CuO:SnO$_2$ (1:1) films is shown in Fig. 6. The transmittance of as-deposited CuO:SnO$_2$ (1:1) films decreases with increase in the RF power. The average transmittance in the visible region of the CuO:SnO$_2$ (1:1) films deposited at 50 W, 100 W and 150 W are 72%, 36% and 19%, respectively. The decrease in transmittance of the films may be due to the increase in film thickness with RF power. The annealing induced effect gives rise to the slight reduction in
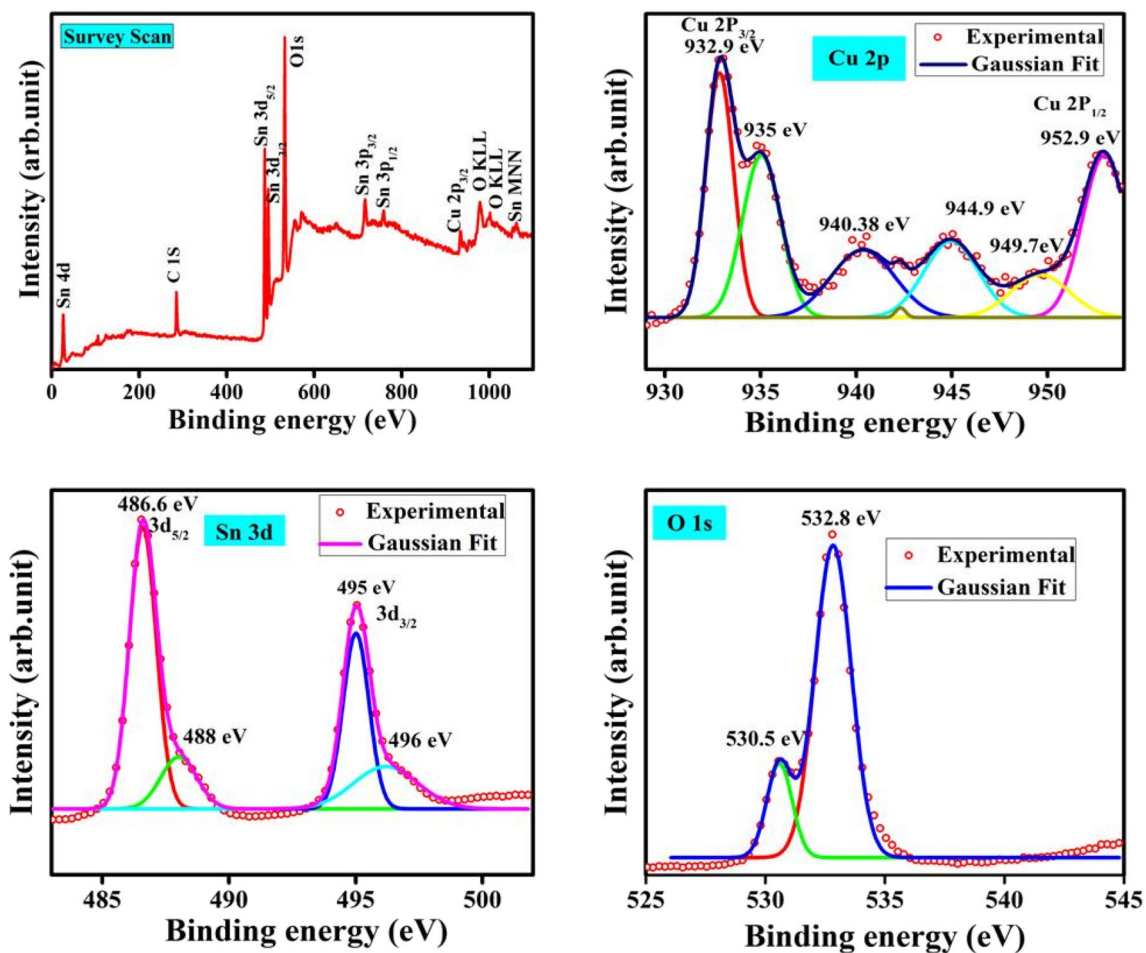

Fig. 5 XPS survey scan and core level (Cu, Sn, O) spectra of CuO:SnO$_2$ thin films prepared with 150 W RF power (annealed at 1000 °C)
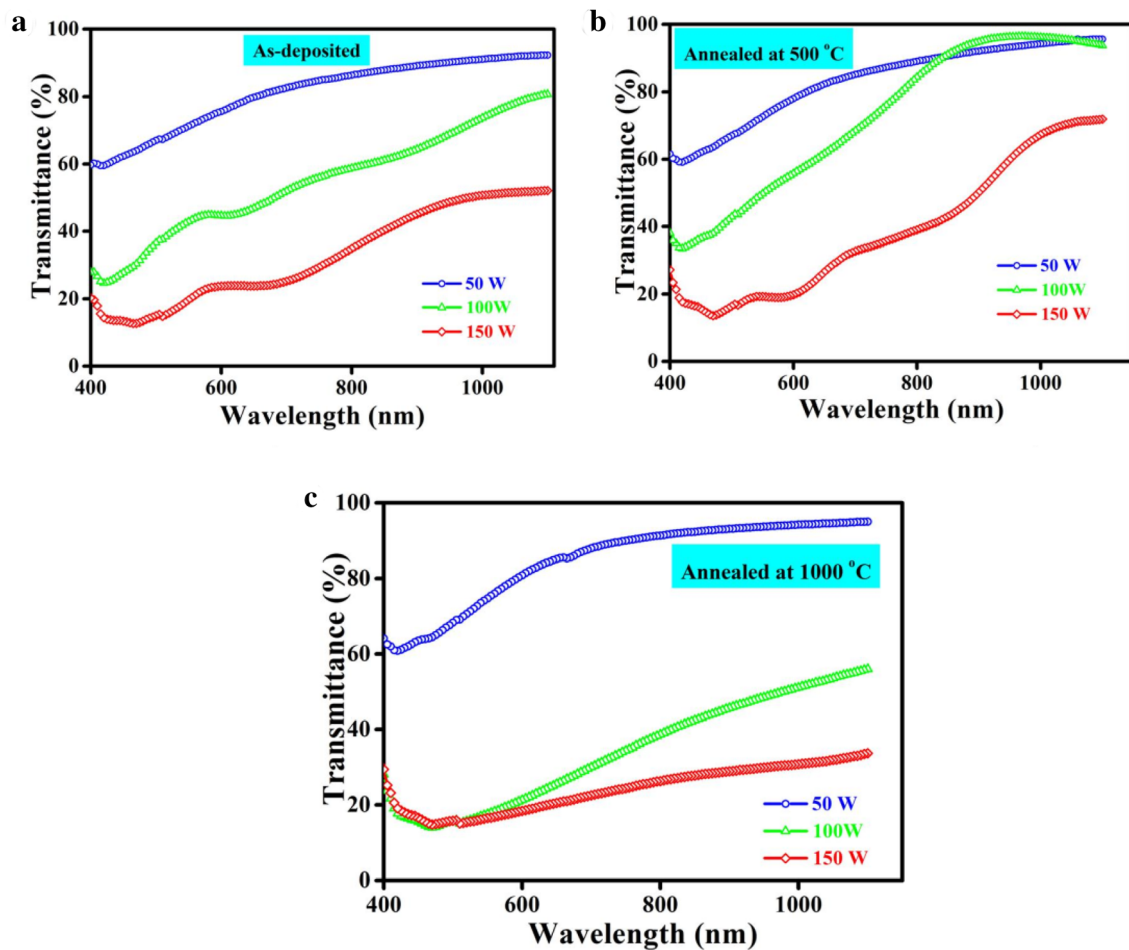
Fig. 6 Effect of RF power on optical transmittance spectra of as-deposited and annealed (at 500 °C and 1000 °C) CuO:SnO$_2$ films prepared with 50 W, 100 W and 150 W RF power

transmittance of the films, which may be due to the improvement in crystallinity of the films [37]. This result is in line with our XRD data, where we observe the crystalline nature of CuO:SnO$_2$ films annealed at 1000 °C.

The optical energy band gaps (E_g) of the films were estimated using Tauc method which is based on the following energy-dependent absorption coefficient equation [38]:

$$\alpha = \frac{B}{h\nu}\left(h\nu - E_g\right)^2 \tag{3}$$

where B is the Tauc coefficient which describes the efficient in light absorption, $h\nu$ is the energy of incoming photons. Figure 7 shows the Tauc plots [between $(\alpha h\nu)^2$ and $h\nu$] of CuO:SnO$_2$ (1:1) films by the effects of RF power and annealing temperature. The extrapolation of the linear region of the Tauc plot to $\alpha = 0$ gives the optical energy band gap and the

estimated energy band gap values are summarized in Table 3. It is observed that the energy band gap of as-deposited and 500 °C annealed films decrease with increasing RF power. This may be due to the formation of localized states near the band edges of CuO:SnO$_2$ film [39]. On the other hand, the energy band gap of 1000 °C annealed CuO:SnO$_2$ film increase with RF power. This may be due to the effect of change in surface morphology and crystallization of the films [40]. In addition, the higher diffusion of oxygen atoms in the films at higher annealing temperature (1000 °C) and the influence of quantum confinement effect caused this variation in energy band gap of CuO:SnO$_2$ film [41].

3.4 Photoluminescence study

The photoluminescence (PL) emission spectra of as-deposited and annealed (at 1000 °C) films are shown

Fig. 7 Optical energy band gap plots of as-deposited and annealed (at 500 °C and 1000 °C) CuO:SnO$_2$ films prepared with 50 W, 100 W and 150 W RF power
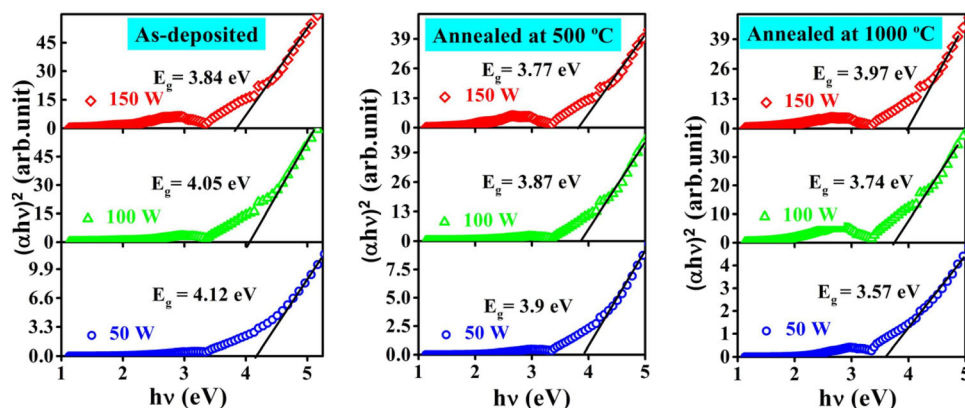

Table 3 Variation of energy band gap values of the CuO:SnO$_2$ (1:1) films by the effect of RF power and annealing temperature

Sample preparation condition	Optical energy band gap (eV)
As-deposited	
50 W	4.12
100 W	4.05
150 W	3.84
Annealed at 500 °C	
50 W	3.90
100 W	3.87
150 W	3.77
Annealed at 1000 °C	
50 W	3.57
100 W	3.74
150 W	3.97

in Fig. 8. All the spectra show peaks at 356 nm, 418 nm, 458 nm and 485 nm. The peak observed at 356 nm is due to the near band edge emission. It may be pointed out that Sial et al. have observed an emission peak around 480 nm for SnO$_2$ nanorods corresponding to the deep trap state of oxygen vacancies [42]. In the deep trap state, trap states were introduced by O^{2-} ions trapping the holes from the valence band. Hence, the emission peak observed in the present work at 485 nm can be assigned to oxygen vacancies. The peaks around 420 nm and 458 nm may be due to the structural defect formed during the deposition of films [43]. The intensities of PL peaks increase with increase in annealing temperature and RF sputtering power, which may be due to the enhancement in crystallinity of the films and film thickness, which in turn leads to the reduction of non-radioactive recombination centers [44].

3.5 FTIR spectroscopic study

FTIR spectra of CuO:SnO$_2$ (1:1) films annealed at 1000 °C are shown in Fig. 9. The absorption peak observed at 470 cm^{-1} is due to the monoclinic phase of CuO and it can be assigned to the stretching vibration of CuO along (101) direction [45]. The longitudinal Eu mode of SnO$_2$ was observed at 669 cm^{-1} [46].

3.6 Electrical property

The electrical properties of the prepared films were analysed with the help of linear four probe arrangement attached to digital source meter. The sheet resistance of the films was calculated at room temperature using the formula [47],

$$Rs = 4.53 \times \left(\frac{V}{I}\right) \tag{4}$$

with appropriate geometric correction $\frac{\Pi}{\ln 2} = 4.53$ [48] and the values are summarized in Table 4. The decrease in sheet resistance with respect to sputtering power is due to the increase in film thickness [49]. It is also noticed from Table 4 that the sheet resistance decreased with increase in annealing temperature which may be due to the grain growth of the films upon annealing treatment [20].

The activation energy of CuO:SnO$_2$ films was evaluated by measuring the variation in electrical resistance with respect to the temperature (27–200 °C). Figure 10 shows the ln(σ) versus 1000/T plots of CuO:SnO$_2$ (1:1) films by the effects of RF power and annealing temperature. The activation energies of the films were calculated using the Arrhenius equation [50],

Fig. 8 Photoluminescence spectra of CuO:SnO$_2$ films deposited at 50 W, 100 W and 150 W RF power
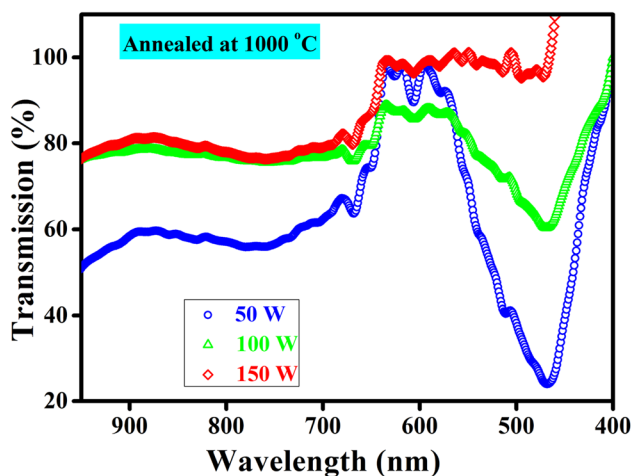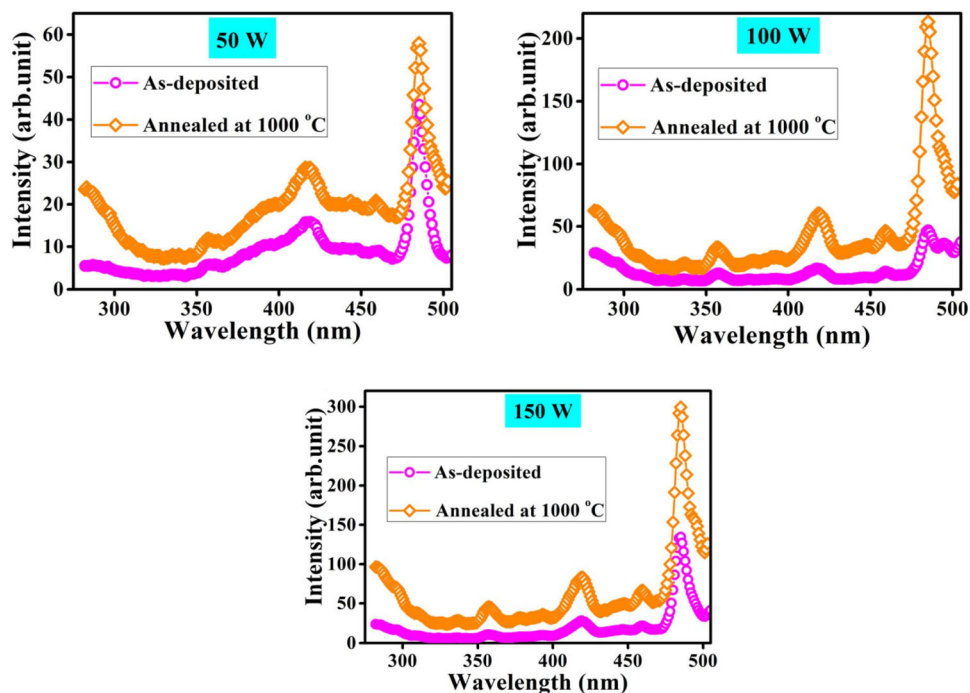

Fig. 9 FTIR spectra of CuO:SnO$_2$ films prepared with 50 W, 100 W and 150 W RF power (annealed at 1000 °C)

$$\sigma = \sigma_o \exp\left(\frac{-E_a}{kT}\right) \quad (5)$$

where σ is the conductivity of the film, σ_o is the temperature independent factor, k is the Boltzmann's constant, and T is absolute temperature. The obtained activation energy values are also presented in Table 4. The activation energy obtained from the graph is found to be decreased with an increase in RF power and annealing temperature. The maximum

activation energy of 3.96 eV was obtained for the film deposited with 50 W RF power. The film deposited at 150 W RF power and annealed at 1000 °C showed minimum activation energy of 0.19 eV. The increase in thickness of the film due to RF power and the change in structural parameters and the improvement in crystallite size due to the annealing treatment may be the reasons for the decrease in activation energy [50].

3.7 Gas sensing property

The gas sensing ability of CuO:SnO$_2$ (1:1) films deposited on quartz glass substrates was analysed in the presence of various gas/vapours at room temperature, by monitoring the electrical resistance variation of the films. It is well known that the gas sensing behaviour of mixed metal oxide thin films is mainly depended on morphological structure. In particular, for room temperature ammonia sensing, mixed metal oxide films with rice grain-like morphology of Cr$_2$O$_3$–CuO [19], nanograss-like morphology of Al$_2$O$_3$–CuO [20] and bone-like morphology of Al$_2$O$_3$–Cr$_2$O$_3$ [51] were exhibited good sensing results. Hence, CuO:SnO$_2$ thin films deposited with 150 W RF power (as-deposited and annealed films) were used for the gas sensing study, since they exhibited dew-like particles and

Table 4 Variation in the sheet resistance and activation energy values of CuO:SnO$_2$ films by the effects of RF power and annealing temperature

Sample preparation condition	Sheet resistance $\times 10^6$ Ω/sq	Activation energy (E_a) (eV)
As-deposited		
50 W	28	3.96
100 W	27	0.68
150 W	6.2	0.45
Annealed 500 °C		
50 W	22	2.58
100 W	20	0.53
150 W	36	0.39
Annealed 1000 °C		
50 W	22	0.32
100 W	19	0.25
150 W	24	0.19

cylindrical-like nanostructures. These nanostructures will provide supplementary reaction locations for oxygen/ammonia gas molecules to absorb/desorb.

3.7.1 Selectivity

The ability of a sensor to respond to a certain gas in the presence of other gases can be defined as selectivity [14]. The selectivity of CuO:SnO$_2$ (1:1) film deposited with 150 W RF power (as-deposited and annealed at 1000 °C) was analysed at room temperature (25 °C) in the presence of 50 ppm of various gas analytes such as ethyl alcohol (CH$_3$CH$_2$OH), ammonia (NH$_3$), dimethyl ketone (CH$_3$COCH$_3$), methylbenzene (C$_6$H$_5$CH$_3$) and formaldehyde (HCHO) in the vapour form and the selectivity plot is shown in Fig. 11. The films showed maximum response to ammonia (NH$_3$). The sensor response of the films deposited with 150 W RF power (as-deposited and annealed at 1000 °C) for different gases at 50 ppm concentrations is shown in Fig. 12. Both as-deposited and annealed films show high response to NH$_3$. This high response towards NH$_3$ may be due to the existence of pair valence electrons and the reduced kinetic diameter of NH$_3$ molecules, which may help them to diffuse quickly into the surface of the sensing material [52]. Hence, the sensing capacity of CuO:SnO$_2$ (1:1) films in the presence of NH$_3$ was studied further.

3.7.2 Sensitivity

In order to find the sensitivity of CuO:SnO$_2$ (1:1) films, the electric resistance of the films was measured in the presence of NH$_3$ vapour at various concentrations (i.e., 10 ppm, 25 ppm, 50 ppm, 75 ppm, 100 ppm, 125 ppm and 150 ppm). The variation of resistance of as-deposited and annealed CuO:SnO$_2$ (1:1) films with exposure and removal of NH$_3$ gas of different concentrations are shown in Fig. 13. As the concentration of the vapour increases the resistance of the films decreased. After the removal of the vapour from the chamber, the film regains its original resistance. This is due to the re-adsorption of the oxygen adatoms on the surface of the films after they had been removed by reactions with ammonia [53]. It is observed that both as-deposited and annealed CuO:SnO$_2$ (1:1) films are able to show response to NH$_3$ gas with concentration from 10 to 100 ppm and after this concentration, the films attain saturation in response. This observation reveals that the prepared CuO:SnO$_2$ films are very sensitive to NH$_3$ gas even at very low concentration of 10 ppm. No significant response was observed below 10 ppm.

The key parameter of any gas sensor is the sensor response and it is defined as the ratio of electrical resistance of the sensor in air (R_a) to the electrical resistance of sensor in gas (R_g) [54], the sensor response (SR) of CuO:SnO$_2$ film for NH$_3$ gas was calculated using the formula [25],

$$SR = \frac{R_a}{R_g} \qquad (6)$$

where R_a is the electric resistance of the film in air and R_g is the electrical resistance of the film in NH$_3$ gas. Figure 14 shows the NH$_3$ gas concentration induced variation of sensor response of as-deposited and annealed CuO:SnO$_2$ films. The sensor response of the as-deposited film at 10 ppm is 1.74 and it
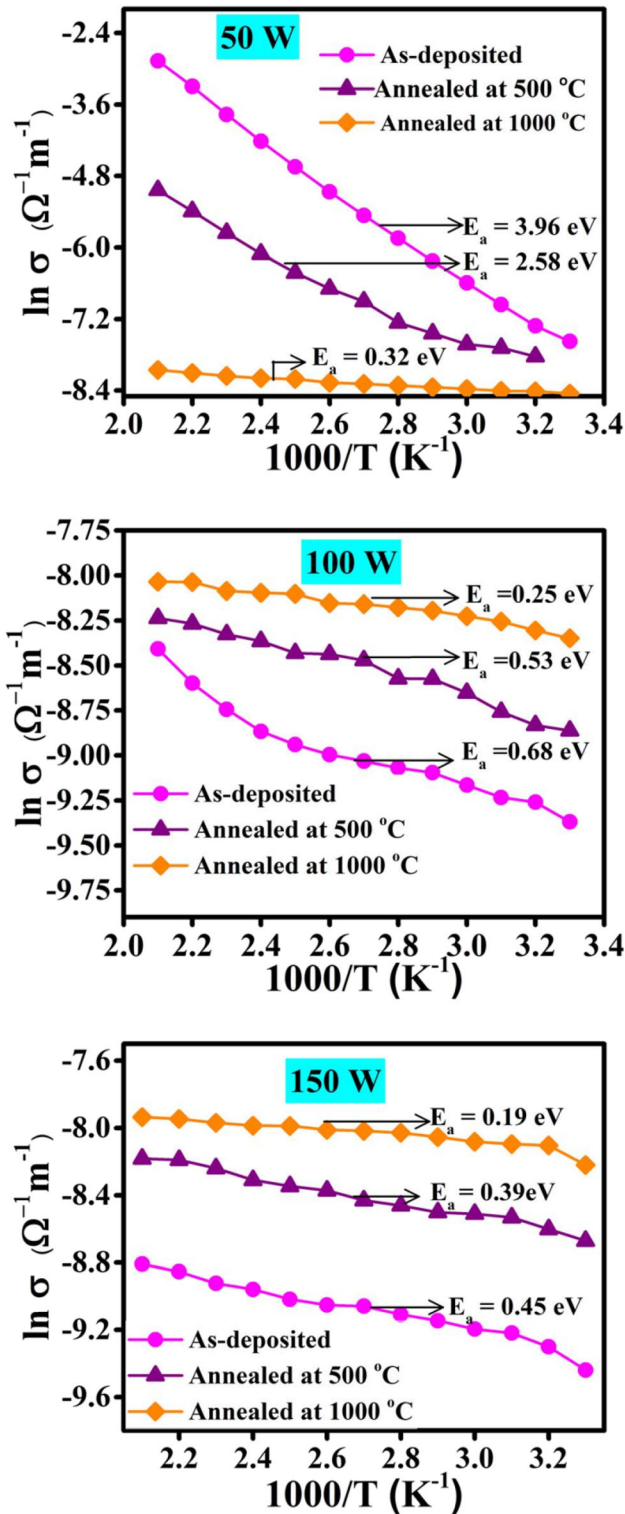
Fig. 10 ln σ versus $1000/T$ plots of CuO:SnO$_2$ films deposited with 50 W, 100 W and 150 W RF power

Fig. 11 Selectivity characteristics of as-deposited and 1000 °C annealed CuO:SnO$_2$ films prepared with 150 W RF power

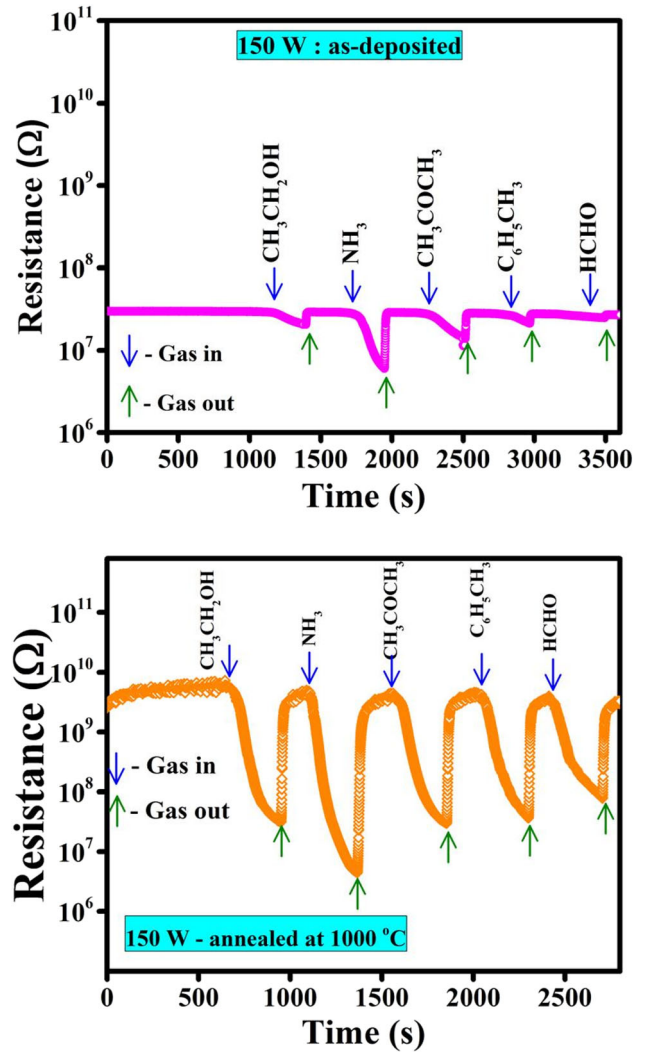increases with increasing concentration of NH$_3$, finally reaches to a maximum value of 11.21 for

100 ppm of NH$_3$, whereas, in the case of annealed film the sensor response increase from 53.24 for 10 ppm to 3838 for 125 ppm. Interestingly, the film annealed at 1000 °C shows a remarkable enhancement in sensor response. This may be due to the rate of adsorption of NH$_3$ gas becomes greater owing to the increase in number of adsorption sites of oxygen species (O$^-$) at the increased surface area and roughness of annealed film [55]. In addition, the sensing response of any reducing gas increases with increase in film thickness [56]. This inference is consistent with our observation where we observe the maximum sensor response for the film annealed at 1000 °C having the thickness of 859 nm. Table 5 shows the comparison of sensor response of the present work with the reported literatures
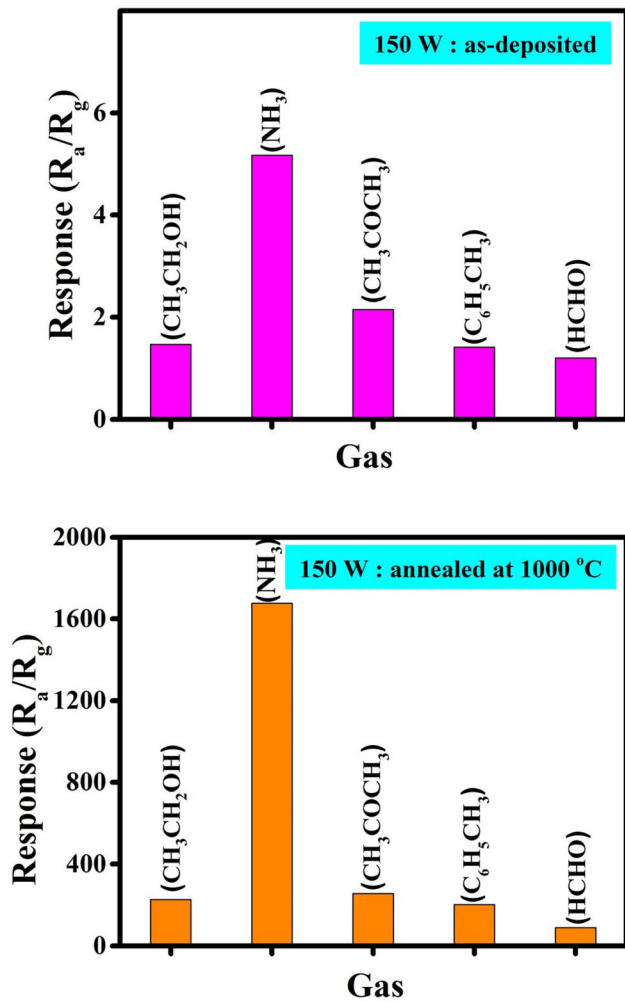
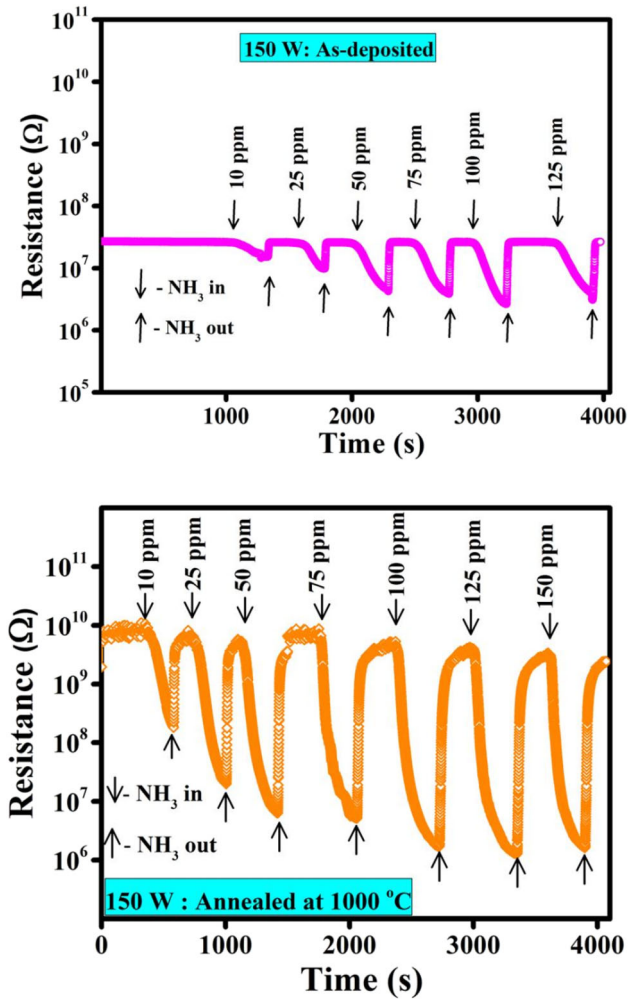**Fig. 12** Sensor response of as-deposited and annealed (1000 °C) CuO:SnO$_2$ films prepared with 150 W RF power for different gases at 50 ppm concentration

Fig. 13 Sensitivity characteristics of as-deposited and annealed (1000 °C) CuO:SnO$_2$ films prepared with 150 W RF power

[2, 6, 57–60], which confirmed the realization of highest sensor response for NH$_3$ gas in the present system (CuO:SnO$_2$ film).

3.7.3 Response/recovery time

Generally, response time (t_{res}) and recovery time (t_{rec}) are most vital parameters in any gas sensor. Response time is measured as the time taken by the sensor to reach 90% of its maximum gas response upon the purging of analyte gas in the test chamber and recovery time is the time taken by the sensor to reach 10% of the maximum response value upon the removal of gas [61]. The response time and recovery time characteristics of as-deposited film for 100 ppm and annealed film for 125 ppm are shown in Fig. 15.

The response time (t_{res}) and recovery time (t_{rec}) of as-deposited CuO:SnO$_2$ films are varied as 162 s and 20 s, respectively, for 100 ppm of NH$_3$. Whereas, in the case of annealed film, the t_{res} is 266 s and t_{rec} is 35 s for 125 ppm of NH$_3$. In order to have better insight in t_{res} and t_{rec} of as-deposited and annealed CuO:SnO$_2$ films by the effect of different concentrations of NH$_3$ gas, the authors have compiled the data as shown in Fig. 16. This change in response time corresponding to the gas concentration may be attributed to the oxygen vacancies present in the film structure [62]. On the removal of NH$_3$ gas, both the as-deposited and the annealed CuO:SnO$_2$ films were returned to their base line with less recovery time. The recovery time is increased from 15 to 22 s and from 10 to 35 s upon increasing the concentration of NH$_3$ gas for the as-deposited and annealed
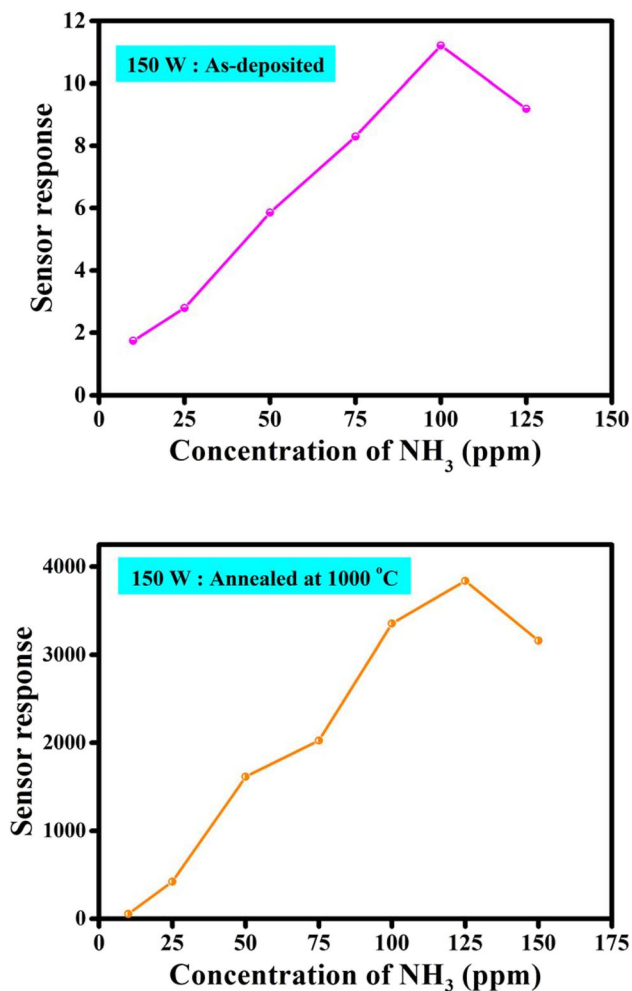
Fig. 14 Sensor response of as-deposited and annealed (1000 °C) CuO:SnO$_2$ films prepared with 150 W RF power for different concentrations of NH$_3$ gas at room temperature

Fig. 15 Response time and recovery time characteristics of NH$_3$ gas for as-deposited and annealed CuO:SnO$_2$ films

CuO:SnO$_2$ films, respectively. The decreased response time and increased recovery time with respect to the increase in concentration of NH$_3$ gas for
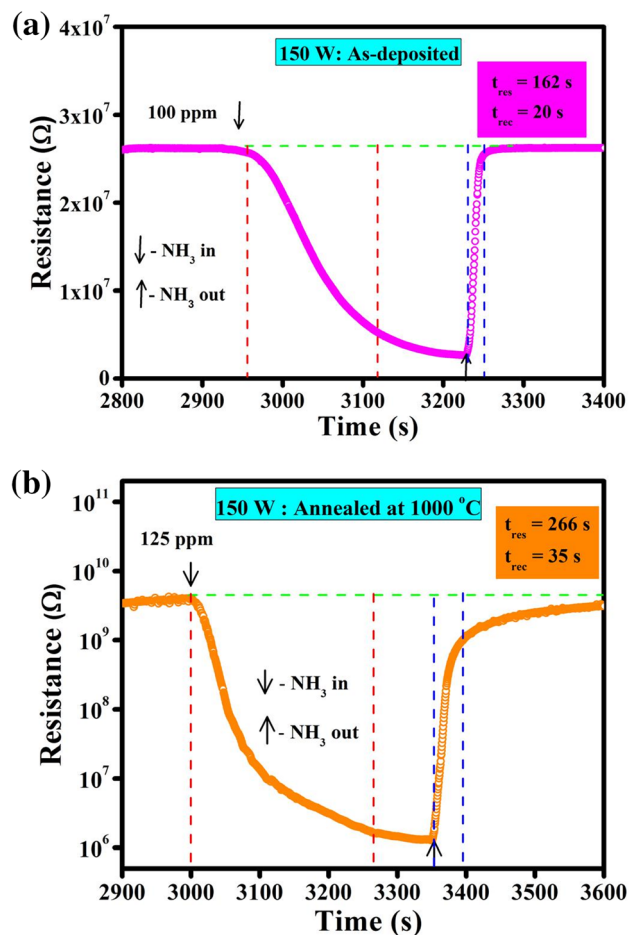
the as-deposited film may be attributed to the fact that at high NH$_3$ concentration, more number of NH$_3$ molecules can be absorbed on the active site of the surface of the film which leads to the saturated

Table 5 Comparison of sensor response of CuO:SnO$_2$ film for NH$_3$ gas with reported literatures

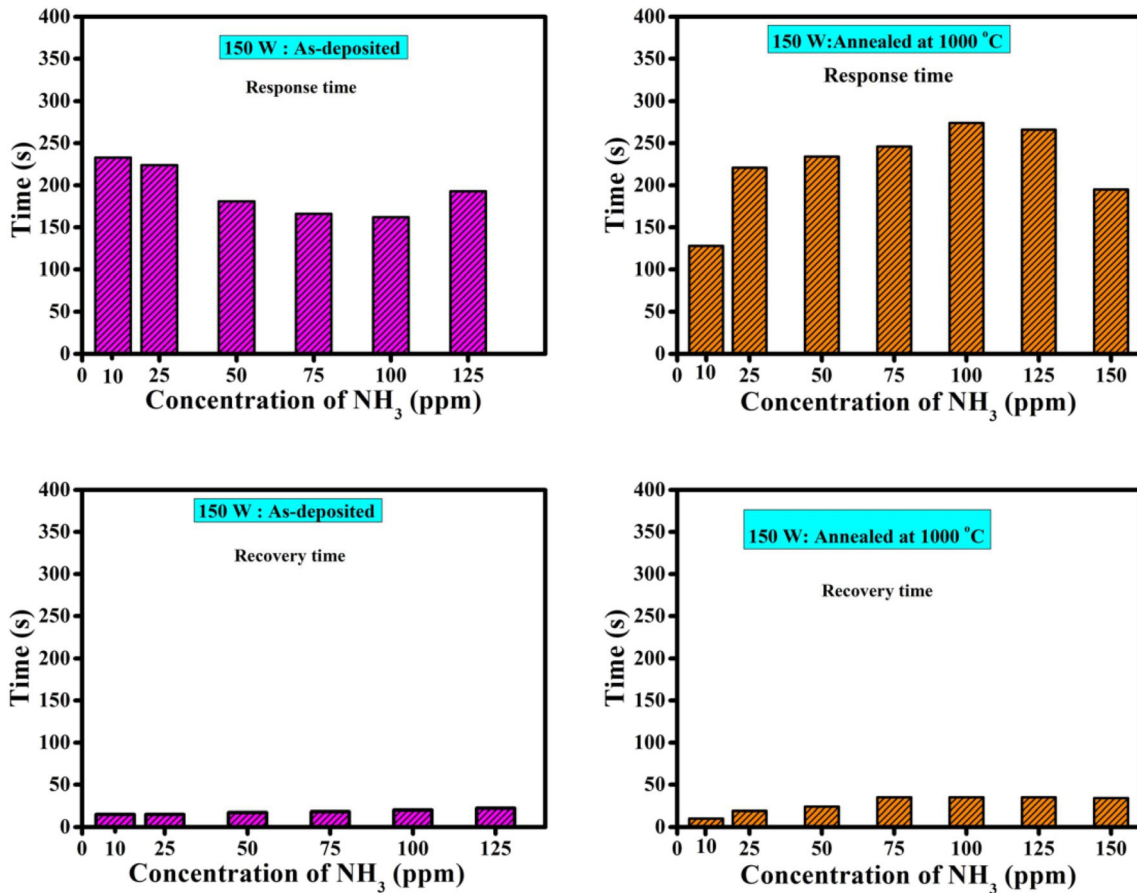| Sensing material	NH$_3$ concentration (ppm)	Operating temperature (°C)	Sensor response (R_a/R_g)	References
Pd/WO$_3$	50	300	8.6	[6]
WO$_3$/Pt	100	260	3.13	[57]
Co$_3$O4/SnO$_2$	100	200	13.6	[58]
ZnO:Co	100	RT	3.48	[59]
ZnO	100	RT	225	[59]
Al-ZnO/CuO	100	RT	131.1	[2]
n-ZnO/p-NiO	100	RT	6	[60]
CuO:SnO$_2$ (as-deposited)	100	RT	11.21	[This work]
CuO:SnO$_2$ (annealed at 1000 °C)	100	RT	3353	[This work]

Fig. 16 Effect of NH_3 gas concentration on the response time and recovery time of as-deposited and annealed $CuO:SnO_2$ films

resistance of the sensor, whereas, in the case of recovery time, longer time was needed to recover to the baseline after the cut off of the gas [63]. Conversely, the increase in response time and recovery time of the annealed film depend on the time needed for gas molecules to diffuse through the film and it is mainly based on the surface morphology of the film [64].

3.7.4 Stability and repeatability

Long-term stability and repeatability are the two main parameters of a gas sensor in real-time application. Stability of a sensor is its ability to give the reproducible results for a certain period of time. Repeatability of a sensor is the ability to repeat the measurement in the same environment. The variation in resistance of the film deposited with 150 W RF power and annealed at 1000 °C, in the presence of 125 ppm of NH_3 gas after six months for five complete cycles is shown in Fig. 17. We do not observe
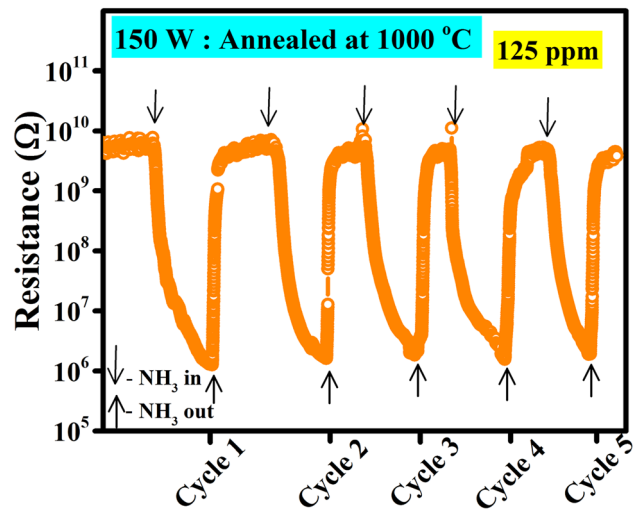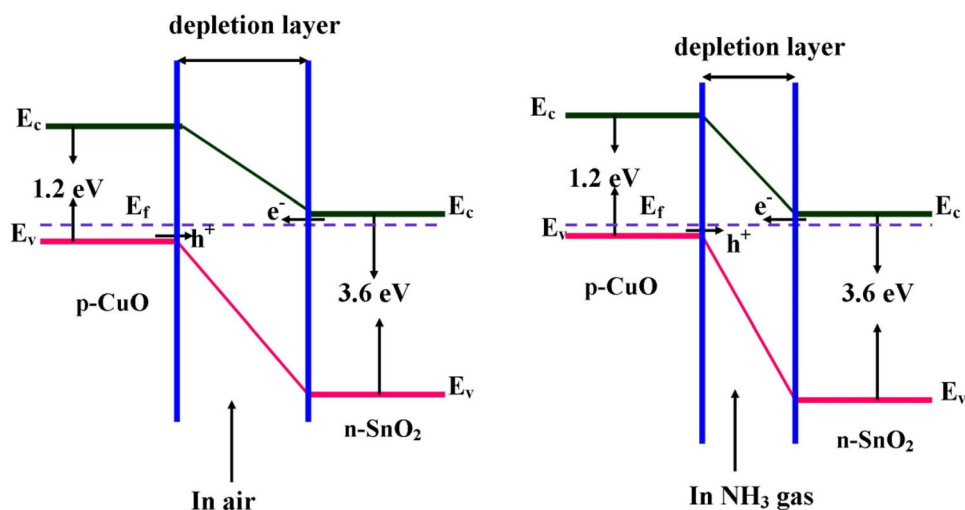

Fig. 17 Repeatability characteristics of annealed (1000 °C) $CuO:SnO_2$ films prepared with 150 W RF power after six months
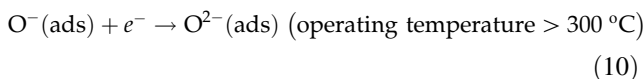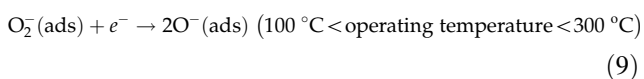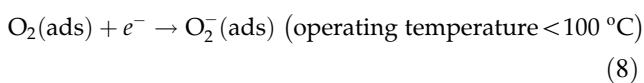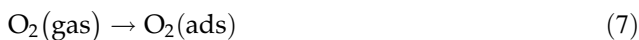
any significant variation in sensor response, which confirmed the stability and repeatability of $CuO:SnO_2$ film in the detection of NH_3 gas.

⚘ Springer

**Fig. 18** Energy band diagram of p-n heterojunction CuO:SnO$_2$

3.7.5 Gas sensing mechanism

The working principle of metal oxide thin film gas sensors is chemoresistance [65], i.e., there will be a change in resistance of the film when the film is exposed to a target gas. When the film is exposed to air, the oxygen present in the air will be adsorbed by the surface of the film. This adsorbed oxygen will capture the electrons from the conduction band of the film and increase the resistance of the film. The oxygen that captured the electrons will be converted into O$_2^-$, O$^-$, and O^{2-} based on the operating temperature, as follows [20],

$$O_2(gas) \rightarrow O_2(ads) \tag{7}$$

$$O_2(ads) + e^- \rightarrow O_2^-(ads) \; (operating\; temperature < 100\; ^\circ C) \tag{8}$$

$$O_2^-(ads) + e^- \rightarrow 2O^-(ads) \; (100\; ^\circ C < operating\; temperature < 300\; ^\circ C) \tag{9}$$

$$O^-(ads) + e^- \rightarrow O^{2-}(ads) \; (operating\; temperature > 300\; ^\circ C) \tag{10}$$

When the target gas molecules come in conduct with the adsorbed oxygen the captured electrons will be released back into the film which in turn increases the conductivity of the film. The CuO:SnO$_2$ mixed composite thin film sensor with high surface roughness can provide more number of adsorption sites for the adsorption of oxygen. Since the sensor is working at room temperature the adsorbed oxygen will be converted into O$_2^-$. When NH$_3$ molecules come in contact with the O$_2^-$ ions they will release the captured electrons and the resistance of the film decreases. The reaction of the NH$_3$ molecule with the adsorbed oxygen is shown below,

$$4NH_3(gas) + 5O_2^- \rightarrow NO + 6H_2O + 5e^- \tag{11}$$
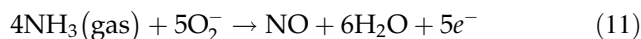
There are two pathways for the formation of nitrogen (N$_2$) gas at RT: one is through NH$_4$NO$_2$ (an intermediate compound) and the other is via a reaction of nitroxyl species with NH$_3$ resulting a diazene (N$_2$H$_2$) species which is further oxidized to nitrogen (N$_2$) and water (H$_2$O) [14, 56].

It is observed that the film annealed at 1000 °C with high surface roughness exhibits a high sensor response. This is because of the fact that the film with high surface roughness will provide more adsorption sites to the oxygen molecule, which in turn leads to capture more number of electrons to form a depletion layer on the surface of the film. This formation of depletion region at the p-n hetrojunction between the surfaces of p-type CuO and n-type SnO$_2$ will also improve the sensor response. When the CuO:SnO$_2$ mixed composite thin film is exposed to NH$_3$ molecules, the oxygen adsorbed on the surface releases the electrons back to the material as shown in Eq. 11. The concentration of the holes in the p-type CuO will be reduced now due to the combination of electrons with the holes, which further reduces the concentration gradient and the depletion region as shown schematically in Fig. 18. As a consequence, the resistance of the film is decreased further. Thus, in the presence of air, the p-n heterojunction greatly increases the resistance and in the presence of NH$_3$ gas, the resistance is decreased, which leads to get the high sensor response [27].

4 Conclusions

In summary, the enhanced gas sensing performance of $CuO:SnO_2$ mixed composite thin film towards NH_3 gas was attained at room temperature. The improved crystalline nature and the surface roughness along with the p-n hetrojunction between the surfaces of p-type CuO and n-type SnO_2 enhanced the sensing property of the film deposited at 150 W RF power and annealed at 1000 °C. The EDX and XPS analyses confirmed the compositional purity of the films and the existence of Cu^{2+} and Sn^{4+} states. The decrease in transmittance of the films may be due to the increase in film thickness with RF power. The FTIR spectra showed the presence of both stretching vibration of CuO and Eu mode of SnO_2 absorption peaks. The gas sensing test confirmed the suitability of the prepared $CuO:SnO_2$ composite film for the detection of NH_3 gas at room temperature operating condition. The maximum sensing response of 3838 was achieved for 125 ppm of NH_3 gas at room temperature. The fast response and recovery time, long-term stability, better repeatability and good sensing performance of $CuO:SnO_2$ composite film confirmed its potentiality for the detection of low concentrate ammonia gas even at room temperature.

References

1. D. Leduc, P. Gris, P. Lheureux, P.A. Gevenois, P.D. Vuyst, J.C. Yernault, Thorax **47**, 755 (1992)
2. M. Poloju, N. Jayababu, M.V.R. Reddy, Mater. Sci. Eng. B **227**, 61 (2018)
3. B. Timmer, W. Olthuis, A. Berg, Sens. Actuators B Chem. **107**, 666 (2005)
4. S. Pawar, M. Chougule, S. Patil, B. Raut, D. Dalvi, P. Patil, S. Sen, P. Joshi, V. Patil, J. Sens. Technol **1**, 9 (2011)
5. S.M. Chou, L.G. Teoh, W.H. Lai, Y.H. Su, M.H. Hon, Sensors **6**, 1420 (2006)
6. C. Castillo, G. Cabello, B. Chornik, Y. Huentupil, G.E. Buono-Core, J. Alloys Compd. **825**, 154166 (2020)
7. S. Büyükköse, Mater. Sci. Semicond. Process. **110**, 104969 (2020)
8. C.F. Li, C.Y. Hsu, Y.Y. Li, NH_3. J. Alloys Compd. **606**, 27 (2014)
9. B. Karunagaran, P. Uthirakumar, S.J. Chung, S. Velumani, E.K. Suh, Mater. Charact. **58**, 680 (2007)
10. M.H. Habibi, N. Talebian, Acta Chim. Slov. **52**, 53 (2005)
11. Y. Zhao, J. Zhang, Y. Wang, Z. Chen, Nanoscale Res. Lett. **15**, 1 (2020)
12. P. Samarasekara, N.T.R.N. Kumara, N.U.S. Yapa, J. Phys. Condens. Matter **18**, 2417 (2006)
13. U.T. Nakate, G.H. Lee, R. Ahmad, P. Patil, Y.B. Hahn, Y.T. Yu, E. Suh, Int. J. Hydrog. Energy **43**, 22705 (2018)
14. S. Ponmudi, R. Sivakumar, C. Sanjeevijara, C. Gopalakrishnan, K. Jeyadheepan, Mater. Res. Express **6**, 066422 (2019)
15. M. Dahrul, H. Alatas, Irzaman, Procedia. Environ. Sci. **33**, 661 (2016)
16. B.J. Wang, S.Y. Ma, Vacuum **177**, 109428 (2020)
17. P.H. Phuoc, C.M. Hung, N.V. Toan, N.V. Duy, N.D. Hoa, N.V. Hieu, Sens. Actuator A. Phys. **303**, 111722 (2020)
18. Y. Xu, L. Zheng, C. Yang, W. Zheng, X. Liu, J. Zhang, A.C.S. Appl, Mater. Inter **12**, 20704 (2020)
19. S. Ponmudi, R. Sivakumar, C. Sanjeeviraja, C. Gopalakrishnan, K. Jeyadheepan, Appl. Surf. Sci. **466**, 703 (2019)
20. S. Ponmudi, R. Sivakumar, C. Sanjeeviraja, C. Gopalakrishnan, K. Jeyadheepan, Appl. Surf. Sci. **483**, 601 (2019)
21. N.F. Habubi, S.F. Oboudi, S.S. Chiad, J. Nano-Electron, Phys. **4**, 4 (2012)
22. X. Xue, L. Xing, Y. Chen, S. Shi, Y. Wang, T. Wang, J. Phys. Chem. C **112**, 12157 (2008)
23. M.K. Verma, V. Gupta, J. Exp. Nano Sci. **8**, 326 (2013)
24. K.R. Park, H.B. Cho, J. Lee, Y. Song, W.B. Kim, Y.H. Choa, Sens. Actuators B Chem. **302**, 127179 (2020)
25. J. Liu, Y. Lu, X. Cui, Y. Geng, G. Jin, Z. Zhai, Sens. Actuators B Chem. **248**, 862 (2017)
26. S.M. Sali, S. Joy, N. Meenakshisundaram, R.K. Karn, C. Gopalakrishnan, P. Karthick, K. Jeyadheepan, K. Sankaranarayanan, RSC Adv. **7**, 37720 (2017)
27. S. Bai, W. GuO, J. Sun, J. Li, Y. Tian, A. Chen, R. Luo, D. Li, Sens. Actuators B Chem. **226**, 96 (2016)
28. M. Meenakshi, V. Gowthami, P. Perumal, R. Sivakumar, C. Sanjeeviraja, Electrochim. Acta. **174**, 302 (2015)

29. X. Yua, J. Maa, F. Jia, Y. Wanga, C. Chengb, H. Maa, Appl. Surf. Sci. **245**, 310 (2005)

30. C.C. Chang, X.D. Wu, R. Ramesh, X.X. Xi, S. Ravi, T. Venkatesan, D.M. Hwang, R.E. Muenchausen, S. Foltyn, N.S. Nogar, Appl. Phys. Lett. **57**, 1814 (1990)

31. P.R. Parmar, M.H. Mangrola, B.H. Parmar, V.G. Joshi, Multi Disciplinary Edu Global Quest **1**, 33 (2012)

32. S. Sujathalekshmy, I.J. Berlin, L.V. Maneeshya, Anitha, K. Joy, IOP Conf. Ser. **73**, 012018 (2015)

33. A. Chaoumead, Y.M. Sung, D.J. Kwak, Adv. Condens. Matter. Phys **651587**, 1 (2012)

34. L. Aruna, C. Karthikeyan, D. Philip, C. Unni, J. Phys. Chem. Solids **136**, 109155 (2020)

35. S. Arunkumar, P. Basak, L. Satyanarayana, Sunkara, V. Manorama, IMCS 372 (2012)

36. G. Li, H. Cui, J. Chen, X. Fang, W. Feng, J. Liu, J. Alloys Compd. **696**, 1228 (2017)

37. S. Abdullahi, A.U. Moreh, B. Hamza, U. Sadiya, Z. Abdullahi, M.A. Wara, H. Kamaluddeen, M.A. Kebbe, U.F. Monsurat, IJIAS **9**, 947 (2014)

38. R. Raciti, R. Bahariqushchi, C. Summonte, A. Aydinli, A. Terrasi, S. Mirabella, J. Appl. Phys. **121**, 234304 (2017)

39. K.S. Usha, R. Sivakumar, C. Sanjeeviraja, J. Appl. Phys. **114**, 123501 (2013)

40. D. Bao, X. Yao, N. Wakiya, K. Shinozaki, N. Mizutani, Appl. Phys. Lett. **79**, 3767 (2001)

41. S. Chuhadiya, R. Sharma, Himanshu, S.L. Patel, S. Chander, M.D. Kannan, M.S. Dhaka, Physica E **117**, 113845 (2020)

42. M.A.Z. Sial, M. Iqbal, Z. Siddique, M.A. Nadeem, M. Ishaq, A. Iqbal, J. Mol. **1144**, 355 (2017)

43. B. Rehman, N.K. Bhalla, S. Vihari, S.K. Jain, P. Vashishtha, G. Gupta, Mater. Chem. Phys. **244**, 122741 (2020)

44. R.L. Orimi, M. Maghouli, Optik **127**, 263 (2016)

45. S. Joshi, S.J. Ippolito, S.V. Manorama, RSC Adv. **6**, 43672 (2016)

46. S. Luo, P.K. Chu, Appl. Phys. Lett. **88**, 183112 (2006)

47. R. Bhattarai, S.P. Shrestha, Am. J. Phys. **5**, 60 (2017)

48. M.A.S. García, A. Maldonado, L. Castañeda, R.S. González, M.D.L.L. Olvera, Mater. Sci. Appl **3**, 690 (2012)

49. K. Tonook, K. Shimokawa, O. Nishimura, Thin Solid Films **411**, 129 (2002)

50. D.L. Kamble, N.S. Harale, V.L. Patil, P.S. Patil, L.D. Kadam, J. Anal. Appl. Pyrol **127**, 38 (2017)

51. S. Ponmudi, R. Sivakumar, C. Sanjeeviraja, C. Gopalakrishnan, J. Mater. Sci. Mater. Electron. **31**, 10123 (2020)

52. Y. Vijayakumar, P. Nagaraju, V. Yaragani, S.R. Parne, N.S. Awwad, Phys. B **581**, 411976 (2020)

53. V.X. Hien, J.H. Lee, J.J. Kim, Y.W. Heo, Sens. Actuators B **194**, 134 (2014)

54. N. Hongsith, E. Wongrat, T. Kerdcharoen, S. Choopun, Sens. Actuators B **144**, 67 (2010)

55. M. Shahabuddin, A. Sharma, J. Kumar, M. Tomar, A. Umar, V. Gupta, Sens. Actuators B **194**, 410 (2014)

56. R. Pandeeswari, B.G. Jeyaprakash, Sens. Actuators B **195**, 206 (2014)

57. M. Stankova, X. Vilanova, J. Calderer, E. Llobet, J. Brezmes, I. Gracia, C. Cane, X. Correi, Sens. Actuators B **113**, 241 (2006)

58. L. Wang, Z. Lou, R. Zhang, T. Zhou, J. Deng, T. Zhang, A.C.S. Appl. Mater. Interfaces **8**, 6539 (2016)

59. G.K. Mani, J.B.B. Rayappan, Mater. Sci. Eng. B **191**, 41 (2015)

60. K. Lokesh, G. Kavitha, E. Manikandan, G.K. Mani, K. Kaviyarasu, J.B.B. Rayappan, R. Ladchumananandasivam, J.S. Aanand, M. Jayachandran, M. Maaza, IEEE Sens. J. **8**, 2477 (2016)

61. M.A. Patil, V.V. Ganbavle, K.Y. Rajpure, H.P. Deshmukh, S.H. Mujawar, Mater. Sci. Energy Technol. **3**, 36 (2020)

62. S. Kanaparthi, S.G. Singh, Mater. Sci. Energy Technol. **3**, 91 (2020)

63. C.M. Hung, D.Q. Dat, N.V. Duy, V.V. Quang, N.V. Toan, N.V. Hieu, N.D. Hoa, Mater. Res. Bull **125**, 110810 (2020)

64. J.C. Hsieh, C.J. Liu, Y.H. Ju, Thin Solid Films **322**, 98 (1998)

65. P. Shankar, J.B.B. Rayappan, Sci. Lett. J. **4**, 126 (2015)